

Contrast mechanisms for the detection of ferroelectric domains with scanning force microscopy

Tobias Jungk, Ákos Hoffmann and Elisabeth Soergel¹

Institute of Physics, University of Bonn, Wegelerstraße 8, 53115 Bonn, Germany

E-mail: soergel@uni-bonn.de

New Journal of Physics **11** (2009) 033029 (14pp)

Received 7 November 2008

Published 25 March 2009

Online at <http://www.njp.org/>

doi:10.1088/1367-2630/11/3/033029

Abstract. We present a full analysis of the contrast mechanisms for the detection of ferroelectric domains on all (x , y and z) faces of bulk single crystals using scanning force microscopy. The experiments were carried out with hexagonally poled lithium niobate to ensure access to a well-defined domain structure on every crystal face. The domain contrast can be attributed to three different mechanisms: (i) the thickness change of the sample due to an out-of-plane piezoelectric response (standard piezoresponse force microscopy), (ii) the lateral displacement of the sample surface due to an in-plane piezoresponse and (iii) the electrostatic tip-sample interaction at the domain boundaries caused by surface charges on the crystallographic y - and z -faces. A careful analysis of the movement of the cantilever with respect to its orientation relative to the crystallographic axes of the sample allows clear attribution of the observed domain contrast to the driving forces.

¹ Author to whom any correspondence should be addressed.

Contents

1. Introduction	2
2. Experimental methods	3
2.1. Movements of the cantilever	4
2.2. Sample rotation stage	4
2.3. Friction between the tip and the sample	5
2.4. Crosstalk compensation	5
2.5. Sample properties and sample preparation	6
3. Movements of the sample surface underneath the tip	7
4. Experimental results and discussion	9
4.1. Imaging of all faces of LiNbO ₃	9
4.2. Lateral imaging of the y -face of LiNbO ₃	12
5. Conclusions	12
Acknowledgments	13
References	13

1. Introduction

Ferroelectric materials are attracting increasing attention owing to numerous applications such as frequency doubling via quasi-phase matching [1], high-speed laser beam deflection [2] or ultrahigh density data storage [3]. These applications require the controlled structuring of the materials with ferroelectric domains, in which the typical size varies from a few microns down to a few nanometers. The performance of the above-mentioned devices strongly depends on the accuracy of the domain patterns, and that is why a non-invasive imaging method with good lateral resolution is highly desirable. In the last 15 years, piezoresponse force microscopy (PFM) has become a standard technique for mapping ferroelectric domains [4, 5]. This is mainly because of its ease of use and high lateral resolution of <20 nm without any special sample preparation [6]. The detection of ferroelectric domain patterns with PFM is based on the fact that ferroelectric materials are necessarily piezoelectric [7]. For PFM, a scanning force microscope (SFM) is operated in contact mode with a voltage applied to the conductive tip. This voltage causes local thickness changes of the ferroelectric sample underneath the tip via the converse piezoelectric effect. The tip follows these thickness changes leading to a deflection of the cantilever that can be read out with a segmented photo-detector.

In contrast with other visualization techniques for ferroelectric domains [8], PFM is not restricted to specific crystallographic orientations. Recording the torsion of the cantilever, thereby revealing an in-plane movement of the sample surface, also enables mapping of domain structures on crystal faces which do not exhibit an out-of-plane response due to thickness changes of the sample [9]. To obtain full information on the domain structure of the sample, it is essential to record deflection and torsion of the cantilever simultaneously. Furthermore, recording the same area after rotation of the sample by 90° is indispensable, since torsion depends on the orientation of the cantilever with respect to the in-plane driving forces. To draw accurate conclusions from those measurements on the ferroelectric domain structures, however, a detailed analysis of the possible movements of the cantilever is required. Consequently,

measurements on single crystals with a well-defined domain configuration provide a better understanding of the PFM contrast mechanisms.

First experiments simultaneously recording the deflection and the torsion of the cantilever were carried out on bulk barium titanate crystals [10, 11]. Only a few studies on other bulk crystals exhibiting *a*- and *c*-domains have been reported since [12]–[17]. Although the possible deformations of a single crystal owing to the piezomechanical response are known, and even more detailed analytical calculations have been carried out (especially for the situation of PFM) [18], there has not been a quantitative experimental investigation of the surface deformations underneath the tip so far. Also on thin films, several experiments simultaneously recording the deflection and the torsion of the cantilever have been reported [19]–[27]. These materials, however, are not suitable for a deeper understanding of the PFM detection mechanism since the domain orientation of every single grain is not unambiguously known in advance. Note that vector PFM [23] does not fulfil the requirements for obtaining full information on the domain configuration of the sample as it does not imply a second image of the same area after the rotation of the sample by 90° .

In this paper, we present a thorough investigation of PFM imaging on all crystal faces of hexagonally poled lithium niobate (LiNbO_3) crystals. All faces show a distinct domain contrast, which on the *x*- and *y*-faces was found to depend strongly on the relative orientation of the cantilever with respect to the crystallographic axes. We therefore upgraded our PFM set-up with a high-precision PC-controlled rotation stage. Performing angular-dependent measurements of the deflection, torsion and buckling of the cantilever, we determined the origins of the domain contrast on each crystal face.

This paper is organized as follows. We start with a detailed description of the experimental methods (section 2). Then we focus on our explanation of the domain contrast on the *x*- and *y*-faces (section 3). Since this model has not been described so far, this section will be very detailed. The last section (section 4) presents the experimental results obtained for all, i.e. the *x*-, *y*- and *z*-faces of a hexagonally poled lithium niobate crystal. Here, we present angle-dependent measurements (section 4.1) to support our explanation for the domain contrast. Finally, images of the *y*-face are analyzed in more detail, confirming the proposed contrast mechanisms (section 4.2).

2. Experimental methods

For the experiments, we use a commercial SFM modified to allow the application of voltages to the tip, and thus to be utilized for PFM. Therefore, the instrument is operated in contact mode with a voltage U applied to the tip, the rear side of the sample being grounded. Applying an electric field E to a piezoelectric sample of thickness t leads to a piezomechanical deformation $\Delta t = E d t$, with d being the appropriate piezoelectric tensor element. Depending on the direction of E , the sample contracts ($\Delta t < 0$) or expands ($\Delta t > 0$). In the case of the voltage U being applied to the sample with the help of the tip—although the electric field distribution is strongly inhomogeneous—a comparable crystal deformation can be measured as $\int_0^t E ds = U$, but is reduced due to clamping [28]. Since the piezoelectric response of the sample is very small, typically of the order of 10 pm V^{-1} , an alternating voltage is applied to the tip ($U = 5 \text{ V}_{\text{rms}}$, $f = 30\text{--}60 \text{ kHz}$) and the response of the cantilever is read out with the help of a lock-in amplifier. This contrast mechanism is generally used for PFM and will be called ‘standard PFM’ in the following. A more detailed analysis of the technique of PFM can be found elsewhere [4, 5].

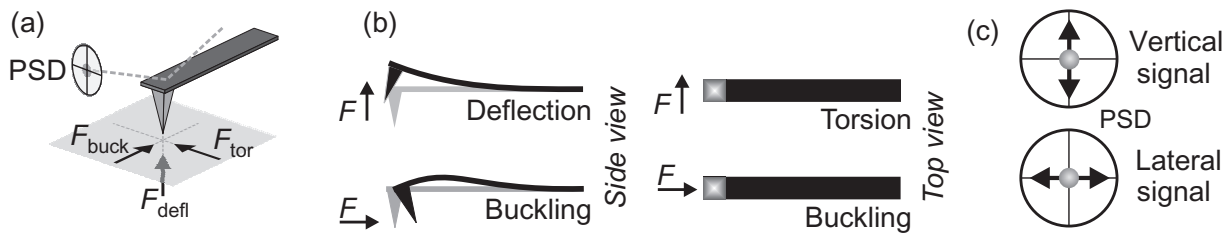


Figure 1. (a) Forces acting on the tip leading to deflection (F_{defl}), torsion (F_{tor}) and buckling (F_{buck}). (b) The out-of-plane force F_{defl} leads to a deflection of the cantilever which is independent of its orientation with respect to the surface normal. For the in-plane forces F_{tor} and F_{buck} , the response of the cantilever depends on its orientation with respect to the driving forces. (c) Deflection and buckling are detected as vertical signals, whereas torsion results in a lateral signal on the position-sensitive detector (PSD).

2.1. Movements of the cantilever

Basically, the cantilever can perform three movements: (i) deflection as a result of an out-of-plane force F_{\perp} acting along the axis of the tip as well as (ii) torsion and (iii) buckling if an in-plane force F_{\parallel} acts perpendicular to the tip (figures 1(a) and (b)). Note that deflection is independent of the orientation of the cantilever with respect to the surface normal. An in-plane force F_{\parallel} acting on the tip perpendicular to the cantilever axis results in torsion, whereas an in-plane force acting along the cantilever axis leads to buckling. Thus, a rotation of the sample by 90° transforms a torsional signal into a buckling signal and vice versa.

Unfortunately, a separate read out of all three signals is not possible since both deflection and buckling are detected in the same read out channel as a ‘vertical signal’ (figure 1(c)). Torsion can, however, be clearly distinguished as it is read out as a ‘lateral signal’. To determine whether a vertical signal is caused by deflection or by buckling, the sample must be rotated. All angular-dependent contributions to the vertical signal can then be attributed to buckling.

2.2. Sample rotation stage

To determine the direction of the in-plane driving force F_{\parallel} acting on the tip, angular-resolved measurements were carried out. We therefore put the SFM on a home-made lifting platform and mounted the sample on a high-precision, PC-controlled rotation stage (Newport URM80). The latter was mounted on top of two piezo-driven translation stages in order to position the rotation axis precisely underneath the tip (figure 2). The obtained accuracy was such that on a full revolution the tip describes a circle of $<3 \mu\text{m}$ radius on the surface. Another set of translation stages, mounted on top of the rotation stage, was used to position the sample underneath the tip. The whole set-up was stable enough to operate the SFM, while rotating the sample. To adjust the pivot of the rotation stage, the displacement of a cross with $20 \mu\text{m}$ wide stripes was watched closely during rotation with the help of an optical microscope. The fine alignment was conducted with a periodically poled LiNbO₃ (PPLN) sample with a domain width of $4 \mu\text{m}$. Comparing two PFM images recorded before and after rotation of the sample by 180° allowed us to determine the misalignment and thereafter to correct it with the piezo-driven translation stages underneath the rotation stage (figure 2). This adjustment had to be repeated for every new cantilever since its mounting is not precise to an accuracy of a few microns.

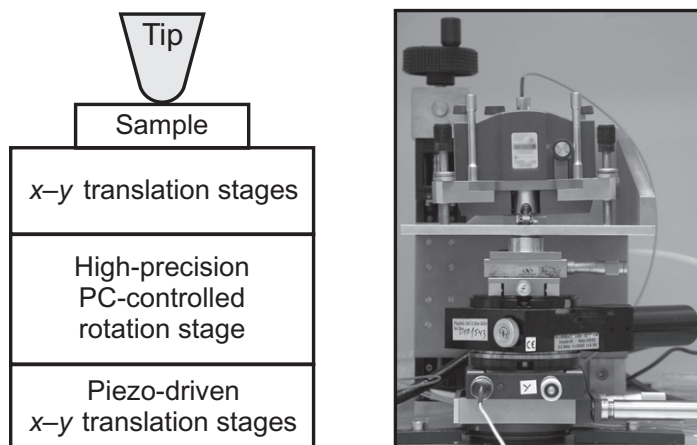


Figure 2. Schematics (left) and photo (right) of the set-up for angular-dependent measurements. The piezo-driven translation stages at the bottom allow a precise positioning of the rotation axis with respect to the tip. The translation stages on top of the rotation stage are used to position the sample.

This set-up allowed us to record SFM images at specific angles between the cantilever and the crystallographic axes of the sample. The adjustment of the cantilever axis with respect to the crystallographic axes was performed by recording large PFM images of PPLN and is precise to about 1° . Furthermore, we performed angular-dependent measurements with the tip stationary, referred to as ‘rotation scans’ in the following. These scans were carried out with the help of a LabView program controlling the rotation stage as well as the lock-in amplifiers. For data acquisition, we waited 100–1000 ms at every new angular position (10 times the time constant of the lock-in amplifier) to let the microscope calm down after the braking of the rotation stage.

2.3. Friction between the tip and the sample

Whenever in-plane forces are present, the question of how these forces are transferred to the tip arises. Thus special attention has to be paid to the friction between tip and sample surface. Therefore, we realized a test set-up depicted in figure 3(a), where we mounted a single-domain LiNbO_3 crystal on top of a shear piezo driven with an alternating voltage U_{AC} . We grounded the tip and the top side of the shear piezo to avoid additional electrostatic forces between the tip and the sample. In this set-up, only in-plane forces act on the tip, resulting in torsion and/or buckling of the cantilever, depending on the relative orientation between the sample movement and the cantilever axis (figure 3(b)). The tip was found to follow the surface movement perfectly for a frequency of $f < 100$ kHz and an amplitude of $A < 300$ pm. Within this parameter regime, the in-plane displacement of the surface is perfectly transferred to the cantilever without any onset of sliding.

2.4. Crosstalk compensation

The aim of attributing the measured signals accurately to the respective driving forces requires a crosstalk-free detection of the vertical and the lateral signals. Usually, the two signals are not fully separated due to a misalignment between the plane of the read-out laser beam and

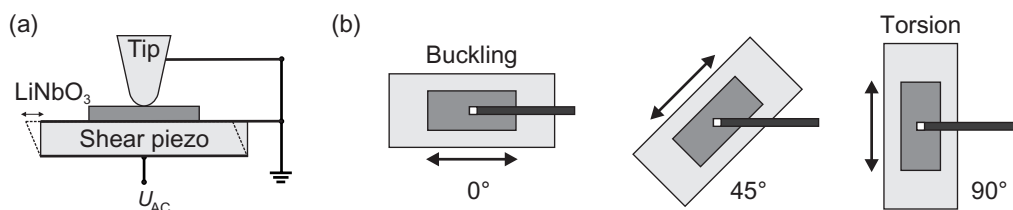


Figure 3. (a) Test set-up for determining the friction between the tip and the LiNbO₃ crystal surface. (b) The transition from buckling to torsion upon rotation of the sample is shown for three selected directions of sample movement relative to the cantilever axis.

the orientation of the position sensitive detector. The set-up with the shear piezo can be used to adjust for the crosstalk, while the tip is in contact with the sample. Torsion and buckling can be excited separately by adjusting the direction of the shear piezo movement relative to the cantilever axis with the help of the rotation stage. False signals caused by crosstalk are then corrected with an electronic circuit [29]. This method of crosstalk compensation is advantageous insofar as it is performed under the same conditions as the measurements carried out later on (contact mode, bent cantilever and outstretched SFM piezo tube).

2.5. Sample properties and sample preparation

The experiments were carried out on congruent lithium niobate (LiNbO₃) crystals. Here, we briefly summarize the crystal's relevant properties. LiNbO₃ belongs to the point-group 3m [7]. The piezoelectric coefficients can be found in [30]: $d_{22} = 21 \text{ pm V}^{-1}$, $d_{33} = 7 \text{ pm V}^{-1}$, $d_{15} = 69 \text{ pm V}^{-1}$ and $d_{31} = -1 \text{ pm V}^{-1}$. These values were determined for bulk crystals in a homogeneous electrical field, i.e. samples covered with large electrodes. In the case of PFM, however, one electrode is realized by the tip leading to a strongly inhomogeneous electric field inside the crystal. As a consequence, clamping occurs [28]. To obtain useful values for this geometry, we determined the ratio of the piezomechanical responses of the y - and z -faces directly by PFM using single-domain samples cut out of y - and z -cut wafers. The ratio was found to be $d_{22} : d_{33} = 1 : 5$. Interestingly, this ratio is $d_{22} : d_{33} = 3 : 1$ using the values from [30] for the case of a homogeneous electric field.

The nominal value for the surface polarization charge on the z -face of LiNbO₃ is 0.7 C m^{-2} [30]. However, compensation of the charges takes place, which is assumed [31] and experimentally verified [32] to be of the order of 1000 under ambient conditions. Indeed, we have evidence for a domain-specific surface charging also on the y -face. Firstly, we measure a strong force between the charged tip and the sample surface at distances $> 10 \mu\text{m}$. We attribute this long-range force to electrostatic interaction. Note that neither on glass nor on the x -face of LiNbO₃ is similar behavior observed during tip sample approach. Secondly, the lateral signal at the domain boundaries on the y -face (sections 4.1 and 4.2) implies a domain-specific surface charging [32]. From comparative measurements, we believe the surface charging on the y -face to be $\frac{1}{3}$ to $\frac{1}{4}$ as large as on the z -face. Although y -face charging has not been explicitly reported so far, it has already been observed [33] and it is also possible from theoretical considerations [34].

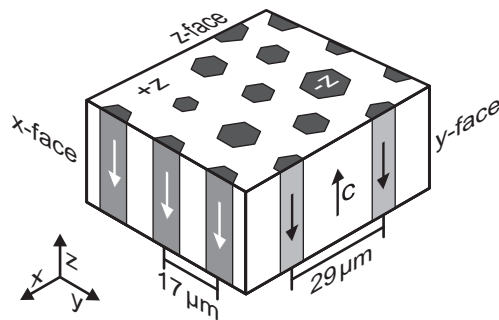


Figure 4. Schematics of the hexagonally poled LiNbO₃ (HexLN) sample used for the investigations. The periodicity of the corresponding domain structures on the side faces is indicated, together with the orientation of the polar c -axis.

For the experiments, we used a hexagonally poled LiNbO₃ (HexLN) crystal as depicted in figure 4. All faces were optically polished. The different period lengths of the domain structures on the x - and y -faces allow an unambiguous identification of the face under investigation. The sample size was $(5 \times 7 \times 0.5) \text{ mm}^3$. To exclude effects from a possible misorientation of the sample cuts relative to the crystallographic axes, we also prepared samples where half of the x - and y -faces were polished at angles of 5° and 10° . The slants, however, did not affect the results significantly.

During the experiments it turned out that special care has to be taken of the mounting of the sample. Any local variation of the grounding electrode was observed to have an influence on the measurements, presuming an angular dependence of the signals measured when rotating the sample. For this reason, the side faces (x and y) were investigated with the sample mounted upright between two plastic (not metal!) brackets. For the measurements on the z -face, the crystal was placed on a large grounded metal plate with 2 cm diameter.

3. Movements of the sample surface underneath the tip

Applying a voltage U to the tip results to a first approximation in a radial field distribution if the tip is described by a sphere. Usually in PFM, only the out-of-plane component E_\perp of the electric field, perpendicular to the sample surface and thus along the axis of the tip, is taken into account, causing a thickness change of the sample. A few publications also discuss shear deformations of the sample caused by E_\perp [10, 16, 23, 24, 35]. With a few exceptions [18, 36, 37], the in-plane components E_\parallel of the electric field, parallel to the sample surface, are generally neglected as they are presumed to cancel out because of the rotational symmetry of the electric field. This argument, however, does not hold in general. The contributions of the piezoelectric deformations caused by opposed electric field components $\pm E_\parallel$ can add up to a net movement of the surface. Thus, for a full analysis of the deformation of the sample surface, all components of the electric field have to be taken into account. For our analysis, we consider the five principal directions of the electric field, choosing the notation such that they follow the crystallographic axes, i.e. when the tip is on top of an x -face, the electric field component E_\perp is called E_x , and the in-plane components E_\parallel are consistently called $\pm E_y$ and $\pm E_z$.

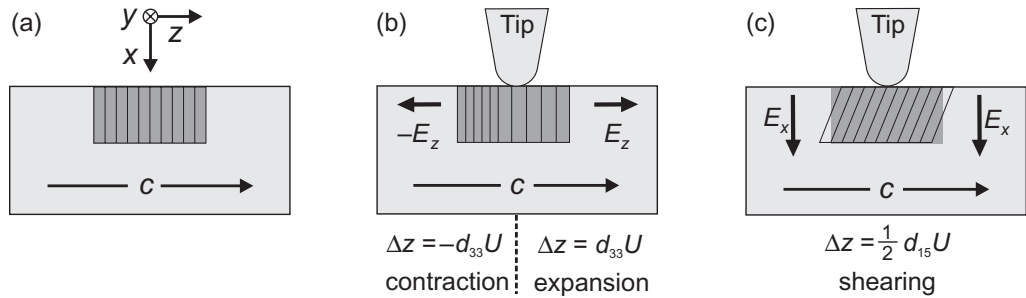


Figure 5. In-plane displacements along the z -axis of a single-domain, x -cut LiNbO_3 crystal underneath the tip. (a) This figure shows the initial situation without the SFM tip. A small volume experiencing later the electric field from the tip is marked in dark grey. The black lines symbolize the crystal lattice planes. In (b) the effect of the electric field components $\pm E_z$ is depicted. The shift of the lattice planes takes place within the limits of the small volume. In (c) the effect of shearing owing to the electric field component E_x is shown. In this case, however, the slanted lattice planes go beyond the limits of the small volume.

In the following, we present a step-by-step analysis of the deformation of the x -face of a single-domain LiNbO_3 crystal underneath the tip when a voltage U is applied to it (figure 5).

- The effect of E_x on the piezoresponse of the sample owing to the longitudinal tensor element d_{11} can be easily calculated since $d_{11} = 0$ for LiNbO_3 , and thus the thickness change is $\Delta x = d_{11} U = 0$.
- The electric field component $+E_z$ causes an expansion along the z -axis ($\Delta z = d_{33} U$), whereas the opposing component $-E_z$ leads to a contraction of the crystal ($\Delta z = -d_{33} U$) by the same amount (figure 5(b)). As a result, an in-plane displacement of the surface underneath the tip along the z -axis occurs. In other words, within a small volume experiencing both electric field components, $+E_z$ on the right and $-E_z$ on the left, the crystal deformation is of two different types (expansion and contraction), which balance each other. Hence, the outer limits of the small volume remain unaffected (no stress!). These considerations can be adopted for the whole volume of the crystal experiencing the electric field of the tip, as for every volume contracting there exists a corresponding volume expanding by the same amount.
- Analogously, the electric field components $\pm E_y$, together with the longitudinal tensor element d_{22} lead to an in-plane displacement of the surface along the y -axis.
- The effect of E_x on the piezoresponse of the sample owing to the shear tensor element d_{15} is schematically depicted in figure 5(c). Within a small volume experiencing the electric field E_x the crystal deformation is of only one type, e.g. a shear strain to the right. As a consequence, stress occurs at the outer limits of this volume. Because of the surrounding material, however, this deformation will be suppressed. The fact that the electric field E_x decays within the crystal and therefore the limits of the small volume are not rigid does not make any significant difference. This only implies that clamping is dispersed along the decay length of the electric field E_x , but the overall net effect persists.

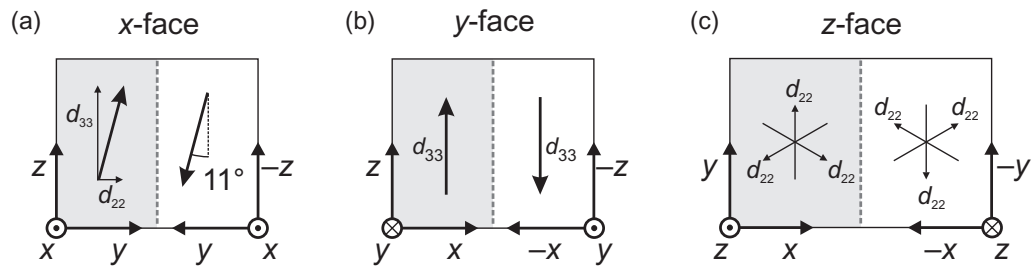


Figure 6. Top view of the in-plane displacements underneath the tip on all faces of a bi-domain LiNbO_3 crystal according to the contraction/expansion model. On the x -face (a) the contributions of d_{22} and d_{33} add up. On the y -face (b) only d_{33} contributes to the displacement ($d_{11} = 0$). On the z -face (c), the three contributions owing to d_{22} cancel out due to the crystal's symmetry.

Figure 6 shows the consequences of the considerations listed above. The x -face performs an in-plane deformation underneath the tip at an angle of $\theta = \arctan(d_{22}/d_{33}) = 11^\circ$ relative to the crystallographic z -axis (figure 6(a)), as can be calculated from the ratio of the piezoelectric tensor elements previously determined by PFM measurements. Note that shearing would lead to a surface displacement at a different angle of $\phi = \arctan(-2d_{22}/d_{15}) = -31^\circ$. Thus, the precise measurement of the direction of the surface displacement is a key experiment to validate the proposed model of contraction/expansion and suppressed shearing.

On the y -face, there is a net thickness change of the sample $\Delta y = d_{22} U$. For the in-plane deformation (figure 6(b)), the same considerations as described above apply. The $\pm E_x$ components of the electric field lead to $\Delta x = d_{11} U = 0$ since $d_{11} = 0$. The $\pm E_z$ components result in an in-plane deformation of the surface along the z -axis ($\theta = 0^\circ$). In this crystal orientation, shearing would lead to a surface displacement at an angle of $\phi = \arctan(-2d_{22}/d_{15}) = -31^\circ$, and again the precise measurement of the direction of the surface displacement is a key experiment to validate the proposed model.

On the z -face, there is a net thickness change $\Delta z = d_{33} U$, yielding the standard PFM signal. Because of symmetry considerations, the three contributions to an in-plane deformation along the crystallographic y -axes should cancel out (figure 6(c)). Note that this argument holds only for a perfect rotationally symmetric electric field, which is difficult to realize in experiments.

4. Experimental results and discussion

4.1. Imaging of all faces of LiNbO_3

Figure 7 summarizes our experimental results. We always recorded the vertical and the lateral signal simultaneously, so (a) and (b), (d) and (e) and (g) and (h) were recorded during the same scan. All images show a clear domain contrast: in (a), (b) and (d) only the domain faces can be seen, in (e) and (h) only the domain boundaries and in (g) a combination of both. On every face, we also performed rotation scans, i.e. the sample was rotated by 360° during data acquisition. For an unambiguous attribution of the recorded signals to the in-plane driving forces, we show the data for the lateral signal in (c), (f) and (i). For the x - and y -faces, the pivot of the rotation axis was set such that the tip performs a circle of a few tens of micrometers radius on top of the

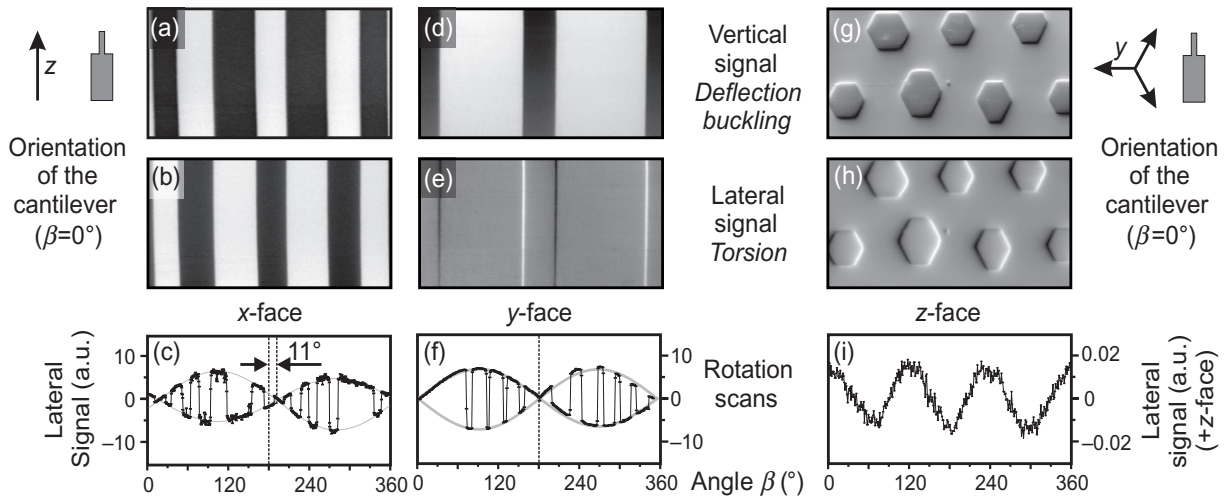


Figure 7. Vertical (a, d, g) and lateral (b, e, h) images ($60 \mu\text{m} \times 30 \mu\text{m}$) of all three faces of the HexLN sample. Bottom row: lateral signal during 360° rotation scans given in arbitrary but identical units. On the x - and y -faces, those rotation scans were performed on the HexLN sample. For the rotation scan on the z -face, we used a single-domain crystal. For the x - and y -faces, β denotes the angle between the axis of the cantilever C and the z -axis of the crystal ($\beta = 0^\circ$: $C \parallel z$). For the z -face, an angle of $\beta = 0^\circ$ corresponds to an orientation of the cantilever perpendicular to one of the three y -axes ($\beta = 0^\circ$: $C \perp y$).

surface, thus crossing several domains during full rotation. Thereby, we recorded the data for both domain faces simultaneously, seen as the two sinusoidal curves connected by the jumps in the graphs. The rotation scan on the z -face was performed on a single-domain LiNbO_3 crystal.

4.1.1. Measurements on the z -face. Investigations of the z -face of the crystal are shown in the last column of figure 7. In the image recorded with the vertical signal (standard PFM), the $-z$ faces of the hexagonal domains appear dark on the bright $+z$ face (figure 7(g)). Furthermore, all domain boundaries are clearly visible, the upper ones in white and the lower ones in black. The image recorded with the lateral signal (figure 7(h)) shows no contrast of the domain faces and reveals only part of the domain boundaries; white on the right, black on the left, but no signal at the top and bottom. We explain the signal at the domain boundaries by the electrostatic interaction between the charged tip and the electric fields perpendicular to the domain walls. The electric field is generated by the differently orientated domains carrying surface polarization charges of opposite polarity. Note that a former assumption where the signal at the domain boundaries was explained via the slope at the domain walls [36, 38] has not been confirmed so far. A detailed analysis of the origin of the lateral signal at the domain boundaries can be found elsewhere [32].

Surprisingly, the rotation scan on the z -face (figure 7(i)) shows a clearly resolvable lateral signal although the contributions of the three identical y -axes were expected to cancel each other out (figure 6(c)). This result can be explained as follows: the tip has an inclination with respect to the surface normal of approximately 20° . The inclination leads to a slight asymmetry of the electric field and thus the contributions from the three y -axes do not exactly cancel

each other out. The three maxima reflect the trigonal symmetry of LiNbO_3 indicating the three crystallographic y -axes. Note that this signal is smaller by a factor of 500 when compared with those on the two other faces (figures 7(c) and (f)).

4.1.2. Measurements on the y -face. Investigations of the y -face of the crystal yield the following results. Figure 7(d) shows the domain faces recorded with the vertical signal. This contrast is produced by both a deflection of the cantilever (standard PFM) and its buckling caused by the in-plane deformation along the z -axis of the crystal. The image recorded with the lateral signal shows only the domain boundaries (figure 7(e)), which we explain, as on the z -face, by electrostatic interaction. This lateral signal at the domain boundaries is a strong indication for the domain-specific surface charging on the y -face.

The rotation scan shows a lateral signal on the domain faces, which is found to be maximal at $\beta = 90^\circ$ (figure 7(f)). Since for a maximum lateral signal, the cantilever must be oriented perpendicular to the driving force (section 2.1), it follows that the in-plane displacement of the surface occurs at $\theta = 0^\circ$ and therefore along the z -axis as was expected from the considerations above (figure 6(b)). This result agrees favorably with the proposed model of contraction/expansion and suppressed shearing.

Note that figure 7(e) only shows the domain boundaries and figure 7(f) only the domain faces, although both were recorded with the same (lateral) signal. This can be understood as follows. Figure 7(e) was recorded at $\beta = 0^\circ$ where the rotation scan in figure 7(f) passes a zero-crossing, i.e. the domain faces are not viewable in the lateral signal. The fact that the rotation scan shows no peaks at the domain boundaries (i.e. at the jumps between the two sinusoidal curves) is due to the limited number of data points recorded. The interplay of the two contributions to the lateral signal on the y -face of the crystal will be presented in detail in section 4.2.

4.1.3. Measurements on the x -face. The experimental results obtained on the x -face of the crystal are shown in the first column of figure 7. In the image recorded with the vertical signal (figure 7(a)), a clear contrast of the domain faces can be seen. Although unexpected on first sight (because $d_{11} = 0$), this can be explained as follows: the in-plane deformation of the surface is expected to occur at an angle of $\theta = 11^\circ$. Thus, recording images with the cantilever oriented along the z -axis ($\beta = 0^\circ$) leads to both buckling (caused by the contribution of d_{33}) and torsion (due to d_{22}). That is why a contrast of the domain faces can be observed with the vertical as well as the lateral signal (figures 7(a) and (b)).

To determine the direction of the in-plane surface displacement on the x -face, we performed the rotation scan shown in figure 7(c). The zero-crossing in the lateral signal was found at $\beta = 11^\circ$. Since for a minimum lateral signal the cantilever must be oriented parallel to the driving force (section 2.1), it follows that the in-plane displacement of the surface occurs at $\theta = 11^\circ$. Again, this result agrees favorably with the proposed model of contraction/expansion and the assumption of suppressed shearing.

As regards a comparison of the experimental data with the analytical calculations from other groups [18], no definitive conclusions can be drawn at the moment. The actual discrepancy between our experimental results and their analytical predictions might be because their model in its present state does not account for any dielectric anisotropy [39].

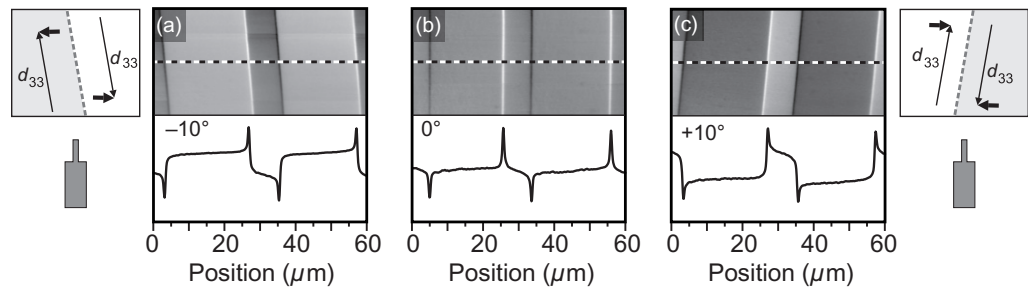


Figure 8. Lateral SFM signal on a y -face of LiNbO_3 recorded for three different angles β between the cantilever and the z -axis: (a) $\beta = -10^\circ$, (b) $\beta = 0^\circ$ and (c) $\beta = +10^\circ$. The graphs below show line scans indicated by the dashed lines in the images. The schemes on the left and on the right illustrate the origin of the lateral signal on the domain faces in (a) and (c). Because of the angle between the movement caused by d_{33} and the cantilever axis, torsion of the cantilever occurs, leading either to a bright (\rightarrow) or to a dark (\leftarrow) contrast of the domain face. For clarity the cantilever, and thus its orientation, is sketched too. The peaks at the domain boundaries are attributed to the electrostatic interaction between the tip and electric fields originating from surface polarization charges.

4.2. Lateral imaging of the y -face of LiNbO_3

The interplay of the two contributions to the lateral signal on the y -face of the crystal caused by the two different contrast mechanisms (in-plane surface displacement along the z -axis ($\theta = 0^\circ$) and electrostatic interaction) can be seen in figure 8. The three images were recorded at different angles β between the cantilever and the z -axis of the crystal. With the cantilever oriented parallel to the z -axis ($\beta = 0^\circ$) only the electrostatic signal at the domain boundaries can be observed (figure 8(b)). Also the line scan shows no contrast of the domain faces. If the sample is rotated, the direction of the in-plane deformation of the surface is no longer parallel to the axis of the cantilever ($\theta = 0^\circ$ but $\beta \neq 0^\circ$) resulting in a lateral signal on the domain faces. Obviously, the contrast on the domain faces is inverted when rotating the sample from $\beta = -10^\circ$ to $\beta = +10^\circ$ (in figure 8(a) the narrow domain is dark, whereas in figure 8(c) the narrow domain is bright). This can be explained as follows: if the response of the sample is in phase with the driving voltage, the lock-in amplifier yields a positive signal, showing up as a bright domain face, and vice versa. During rotation of the sample from $\beta = -10^\circ$ to $+10^\circ$, the direction of the in-plane surface displacement leading to torsion reverts and, consequently, the phase of the response is shifted by 180° , resulting in the inversion of the contrast on the domain faces.

5. Conclusions

In this study, we have carried out a thorough investigation of the origin of the domain contrast on all faces of LiNbO_3 single crystals. A clear domain contrast was observed on all crystal faces. Upon close inspection, we attributed the domain contrast to a superposition of three different mechanisms: (i) standard piezoresponse force microscopy originating from a thickness change of the sample, (ii) a piezomechanically caused in-plane displacement of the surface owing to an expanding/contraction movement and (iii) the electrostatic interaction of the charged tip with the electric fields at the domain boundaries on the crystal's y - and z -faces.

In order to perform these experiments, we upgraded our scanning force microscope, mounting the samples on a high-precision rotation stage. It has thus become possible to investigate a well-defined area at different orientations of the cantilever with respect to the crystallographic axes of the sample. This technical issue in combination with the full understanding of the detection mechanisms now allows us to determine the orientation of the polar axis of any arbitrarily orientated ferroelectric sample.

Acknowledgments

We thank S Mailis for a very helpful measurement and fruitful discussions and C Gawith for providing the HexLN sample, both from the Optoelectronics Research Centre, University of Southampton (UK). Deutsche Telekom AG is gratefully acknowledged for financial support.

References

- [1] Fejer M M, Magel G A, Jundt D H and Byer R L 1992 *IEEE J. Quantum Electron.* **28** 2631
- [2] Scrymgeour D A, Barad Y, Gopalan V, Gahagan K T, Jia Q, Mitchell T E and Robinson J M 2001 *Appl. Opt.* **34** 6236
- [3] Cho Y, Hashimoto S, Odagawa N, Tanaka K and Hiranaga Y 2005 *Appl. Phys. Lett.* **87** 232907
- [4] Alexe M and Gruverman A 2004 *Nanoscale Characterisation of Ferroelectric Materials* 1st edn (Berlin: Springer)
- [5] Jungk T, Hoffmann Á and Soergel E 2006 *Appl. Phys. Lett.* **89** 163507
- [6] Jungk T, Hoffmann Á and Soergel E 2008 *New J. Phys.* **10** 013019
- [7] Newnham R E 2005 *Properties of Materials* 1st edn (New York: Oxford University Press)
- [8] Soergel E 2005 *Appl. Phys. B* **81** 729
- [9] Canalias C, Pasiskevicius V, Fragemann A and Laurell F 2003 *Appl. Phys. Lett.* **83** 734
- [10] Abplanalp M, Eng L M and Günther P 1998 *Appl. Phys. A* **66** S231
- [11] Eng L M, Güntherodt H-J, Schneider G A, Köpke U and Muñoz Saldaña J 1999 *Appl. Phys. Lett.* **74** 233
- [12] Yu H F, Zeng H R, Zhang L N, Chu R Q, Li G R and Yin Q R 2005 *Mater. Lett.* **59** 1538
- [13] Katayama S, Noguchi Y and Miyayama M 2007 *Adv. Mater.* **19** 2552
- [14] Okino H, Ida T, Ebihara H, Yamada H, Matsushige K and Yamamoto T 2001 *Japan. J. Appl. Phys.* **40** 5828
- [15] Amornin H, Shvartsman V V, Bdikin I K, Costa M E V, Kholkin A L and Pertsev N A 2006 *Appl. Phys. Lett.* **88** 062903
- [16] Abplanalp M, Barošova D, Bridenbaugh P, Erhart J, Fousek J, Günther P, Nosek J and Šulk M 2002 *J. Appl. Phys.* **91** 3797
- [17] Zeng H R, Yu H F, Chu R Q, Li G R, Luo H S and Yin Q R 2004 *J. Cryst. Growth* **267** 194
- [18] Eliseev E A, Kalinin S V, Jesse S, Bravina S L and Morozovska A N 2007 *J. Appl. Phys.* **102** 014109
- [19] Zavaliche F, Das R R, Kim D M, Eom C B, Yang S Y, Shafer P and Ramesh R 2005 *Appl. Phys. Lett.* **87** 182912
- [20] Gautier B and Bornand V 2006 *Thin Solid Films* **515** 1592
- [21] Loppacher C, Schlaphof F, Schneider S, Zerweck U, Grafström S, Eng L M, Roelofs A and Waser R 2003 *Surf. Sci.* **532** 483
- [22] Zeng H Z, Liu J S, Dai L S, Wang Z H, Bao S X and Li Y R 2005 *J. Electroceram.* **15** 135
- [23] Kalinin S V, Rodriguez B J, Jesse S, Shin J, Baddorf A P, Gupta P, Jain H, Williams D B and Gruverman A 2006 *Microsc. Microanal. Microstruct.* **12** 206
- [24] Ganpule C S, Nagarajan V, Hill B K, Roytburd A L, Williams E D, Ramesh R, Alpay S P, Roelofs A, Waser R and Eng L M 2002 *J. Appl. Phys.* **91** 1477
- [25] Yu H F, Zeng H R, Chu R Q, Li G R and Yin Q R 2005 *Phys. Status Solidi a* **202** 158

- [26] Shvartsman V V, Kleemann W, Haumont R and Kreisel J 2007 *Appl. Phys. Lett.* **90** 172115
- [27] Rodriguez B J, Gruverman A, Kingon A I, Nemanich R J and Cross J S 2004 *Appl. Phys. Lett.* **95** 1958
- [28] Jungk T, Hoffmann Á and Soergel E 2007 *Appl. Phys. A* **86** 353
- [29] Hoffmann Á, Jungk T and Soergel E 2007 *Rev. Sci. Instrum.* **78** 016101
- [30] Hellwege K-H and Hellwege A M (ed) 1981 *Ferroelectrics and Related Substances (Landolt-Börnstein III/16)* (Berlin: Springer)
- [31] Likodimos V, Labardi M, Allegrini M, Garcia N and Osipov V V 2001 *Surf. Sci.* **490** 76
- [32] Jungk T, Hoffmann Á and Soergel E 2006 *Appl. Phys. Lett.* **89** 042901
- [33] Goulkov M, Odoulov S, Woike T, Imbrock J, Imlau M, Krätzig E, Bäumer C and Hesse H 2002 *Phys. Rev. B* **65** 195111
- [34] Tasker P W 1979 *J. Phys. C: Solid State Phys.* **12** 4977
- [35] Felten F, Schneider G A, Muñoz Saldaña J and Kalinin S V 2004 *J. Appl. Phys.* **96** 563
- [36] Scrymgeour D A and Gopalan V 2005 *Phys. Rev. B* **72** 024103
- [37] Morozovska A N, Eliseev E A, Bravina S L and Kalinin S V 2007 *Phys. Rev. B* **75** 174109
- [38] Wittborn J, Canalias C, Rao K V, Clemens R, Karlsson H and Laurell F 2002 *Appl. Phys. Lett.* **80** 1622
- [39] Morozovska A N 2008 private communication